ADVANCED MATERIALS
www.advmat.de

Thermoelectric Characterization of Bismuth Telluride Nanowires, Synthesized Via Catalytic Growth and Post-Annealing

Bacel Hamdou, Johannes Kimling, August Dorn, Eckhard Pippel, Raimar Rostek, Peter Woias, and Kornelius Nielsch**

Bi_2Te_3-based materials are among the most promising materials for thermoelectric applications with a figure of merit close to 1 near room temperature.[1] Recently, it has been predicted and demonstrated that Bi_2Te_3 is a 3D topological insulator (a phase of matter that has a bulk bandgap and gapless electronic surface states that are protected by time-reversal symmetry).[2–4] Nanostructured Bi_2Te_3 can be beneficial for both research areas. Regarding thermoelectrics, theoretical investigations predict that confinement effects in nanowires (NWs) can strongly enhance the thermoelectric powerfactor.[5] On the other hand, the increased surface-to-volume ratio of NWs magnifies the contribution of surface states to electronic transport, which facilitates experimental access for studying topological insulating materials.[6]

For thermoelectric applications, Bi_2Te_3 needs to be n-type or p-type with a carrier concentration on the order of 10^{19} cm^{-3} for optimal power factors.[1] For studying topological insulator surface states, stoichiometric and therefore intrinsic Bi_2Te_3 is desirable to avoid unwanted bulk conductivity.[2] However, small formation energies of antistructure-type defects pose an interesting materials challenge for achieving control over the structural and electronic properties of bismuth tellurides.[7,8]

Recently, thermoelectric and structural properties have been correlated for the homologous series Bi_2Te_3, Bi_4Te_5, Bi_6Te_7, Bi_8Te_9, BiTe, Bi_4Te_3, Bi_2Te, and Bi_7Te_3.[9] To our knowledge, a synthesis route to bismuth telluride nanowires of well-defined stoichiometry and crystal structure, as well as reproducible thermoelectric properties has not been established. Measurements on individual bismuth telluride NWs have only shown weak thermoelectric performances compared with bulk Bi_2Te_3.[10,11] The most-prominent method for synthesizing bismuth telluride NWs is template-assisted electrodeposition.[12–18] Solution-based chemical methods provide alternative routes to nanowires of group V–VI compounds.[19–21] An efficient and competitive physical method for the fabrication of bismuth telluride nanowires was reported by Ham et al.[22] The vapor-liquid-solid (VLS) method from the gaseous phase, which is a prevalent method for growing wires of a large variety of semiconducting materials (e.g., Si, Ge, and group III–IV compounds),[23,24] has been less frequently applied to group V–VI compounds. Bi_2Se_3, Sb_2Te_3, and Sb_2S_3 NWs have been synthesized via physical[25,26] and chemical[27] vapor deposition. The growth of bismuth telluride nanorods and nanobelts by VLS has been reported by Wang et al.[28] and by Wei et al.,[29] however, no thermoelectric measurements have been performed. In the work of Wang et al.[28] Bi_4Te_3 nanorods with a length on the order of 0.5 μm were grown using a molecular beam epitaxy system. Wei et al.[29] employed thermal evaporation of Bi_2Te_3 powder inside a sealed evacuated quartz tube and obtained flat bismuth telluride nanobelts. Although they assumed that the nanobelts had the composition of Bi_2Te_3, a compositional analysis confirming this assumption was not presented in their work. Recently, Han et al. have demonstrated that electrochemically grown Bi_2Te_3 NWs exhibit a reversible phase change from the crystalline to the amorphous phase, at a critical temperature of about 234 °C.[30] However, as uniaxial VLS-growth of nanowires is based on the growth of single-crystals, the absence of a crystalline phase for Bi_2Te_3 NWs, as observed by Han et al., indicates that this method is not suitable for growing Bi_2Te_3 NWs above 234 °C. On the other hand, for NWs with bismuth contents above 40 at%, this phase change was not observed.[30] A change in the composition from Bi_2Te_3 to Bi_4Te_3 after annealing under Ar atmosphere has been observed for electrodeposited bismuth telluride nanowires, and was attributed to the high vapor pressure of Te.[31] For bismuth telluride thin films it has been demonstrated that Bi-rich phases can be transformed into Bi_2Te_3 by annealing in a Te atmosphere.[32] In this work, we have performed gold-nanoparticle-assisted catalytic VLS-growth of bismuth telluride and obtained NWs with a reduced Te content below 60 at%. By post-annealing in a Te atmosphere, we were able to transform the as-grown NWs to the desired single-crystalline Bi_2Te_3 phase.

The synthesis was performed in a single-heater zone tube furnace (Supporting Information, Figure S1). At the hot center of the furnace, the source material (Bi_2Te_3 powder with 99.99% purity) was thermally evaporated at 470 °C. A constant flow of argon carrier-gas was used to transport the vapor to the substrate where the growth took place. The substrate was covered with gold

B. Hamdou, J. Kimling, Dr. A. Dorn, Prof. K. Nielsch
Institut für Angewandte Physik
Universität Hamburg
Jungiusstr. 11, 20355 Hamburg, Germany
E-mail: johannes.kimling@physik.uni-hamburg.de;
kornelius.nielsch@physik.uni-hamburg.de
Dr. E. Pippel
Max-Planck-Institut für Mikrostrukturphysik Halle
Weinberg 2, 06120 Halle, Germany
R. Rostek, Prof. P. Woias
Institut für Mikrosystemtechnik
Albert-Ludwigs-Universität Freiburg
Georges-Köhler-Allee 106, 79110 Freiburg, Germany

DOI: 10.1002/adma.201202474

nanoparticles (30 nm in diameter), which serve as catalysts for the growth of NWs. The base temperature of 470 °C decreases from the center of the furnace toward its ends. The position of the substrate should correspond to the temperature range within which VLS growth of nanowires occurs. As a reference point for determining this temperature range, the pseudobinary eutectic temperature T_e of the Au-Bi_2Te_3 system can be used, which is 475 °C.[33] However it is known from other important VLS processes that uniaxial NW growth can proceed below T_e. For example, it has been shown for the Au-Ge system that below T_e NWs grow via VLS and vapor-solid-solid (VSS) processes.[34] We observe nanowire growth at temperatures well below T_e. Conditions for uniaxial growth appear to be best at temperatures of about 420 °C. We note that for bulk systems, the crossing of the liquidus surface in this temperature range leads to the nucleation of crystals of the phase BiTe.[33] We observe that the probability for uniaxial growth depends critically on the mass flow of evaporated source material and on the density of gold nanoparticles:

- *mass flow of educts*: The flow rate of evaporated source material through the tube at a given base temperature is determined by its vapor pressure, the surface area of the source material, and the flow rate of the Ar carrier-gas. For large flow rates vapor-solid (VS) growth dominates over uniaxial VLS growth. The growth of larger plates and crystallites, several micrometers in size, is observed.
- *density of gold nanoparticles*: Small distances between adjacent gold nanoparticles and agglomerations of several gold nanoparticles hinder uniaxial growth. The initially catalyzed growth at each seed particle combines to a single object.

Both parameters, the mass flow of educts and the gold-nanoparticle density, were optimized to enhance uniaxial growth of NWs. However, uniaxial growth was always accompanied by two-dimensional and three-dimensional VS-growth (**Figure 1**b,c). In the absence of catalyst particles we observe growth of nanoplates (Supporting Information, Figure S2). Few-layer nanoplates of Bi_2Te_3, synthesized by this method, could be of high importance for the field of topological insulating materials.[35,36] The cross-sectional areas of most of the NWs appear polygonal (Supporting Information, Figure S3a), however, almost-cylindrical NWs are also observed (Supporting Information, Figure S3b). To gain insight into possible growth mechanisms, we compared the distribution of gold nanoparticles with the growth products in the same area after a 5 min deposition of bismuth telluride at 470 °C (Figure 1a,b). The initial locations of the gold catalyst particles shown in Figure 1a are highlighted in Figure 1b with arrows. It can be seen that the gold nanoparticles moved during the growth process. Moreover, the starting points of the NWs coincide with the initial locations of the gold nanoparticles involved in the growth process. This indicates that crystal growth was nucleated at the gold nanoparticles, which are clearly visible at the edges and corners of NWs, and proceeds via the VLS mechanism. Additionally, we observe lateral growth at the side facets of flat NWs (Figure 1c). We conclude that the formation of flat NWs proceeds via uniaxial VLS growth in combination with lateral VS-growth. By comparing of the VLS-grown NW segment with the shorter segment which grew in the opposite direction via a VS process in Figure 1c, it follows that the uniaxial VLS-growth rate exceeds the VS-growth rate by a factor of about 6. However, we do not observe tapered NWs, as could be expected from the VS-growth process. Possible explanations could be the layered crystal structure of bismuth telluride, in combination with a high surface diffusion rate of the adsorbed atoms. After a deposition process of 1 h at a 470 °C base temperature, the NWs reach lengths of up to 15 µm. The thickness of the NWs, which we define as the smallest length perpendicular to the wire axis, ranges from 30 nm to 150 nm. The minimum thickness of 30 nm, observed using scanning force microscopy, corresponds to the diameter of the gold nanoparticles. Statistical distributions of the length scales perpendicular to the wire axis are given in Figure S4 in the Supporting Information. The as-grown NWs were post-annealed in a Te atmosphere at 250 °C for 100 h inside a sealed quartz tube. The actual crystalline state of the nanowires during annealing is unclear. According to Han et al., the nanowires should change to the amorphous state, if the Te content approaches 60 at.% at 250 °C.[30] If this were true, the nanowires could still recrystallize while the temperature is slowly decreased after the annealing step. The chemical composition and crystal structure of both as-grown and annealed NWs were analyzed using element-specific energy-dispersive X-ray (EDX) spectroscopy inside a high-resolution transmission electron microscope (HR-TEM). The accuracy of the employed EDX spectroscopy method lies between 5% and 10%. This accuracy can in principle be improved by using high-accuracy EDX spectroscopy chemical analysis.[17,18] For as-grown nanowires, we obtain a composition of $Bi_{0.46 \pm 0.05}Te_{0.54 \pm 0.05}$, which corresponds to a composition between the Bi_4Te_5, Bi_6Te_7, Bi_8Te_9, and BiTe phases (**Figure 2**a). The specified confidence interval is due to the analysis method. At the surface of the as-grown NWs, we observe a clear increase of the Bi content up to about 60 at.% (Supporting Information, Figure S5).

The selected area electron diffraction (SAED) patterns show a hexagonal lattice (Trigonal, hR15, SpaceGroup R-3m, No.166) (insets of Figure 2c,d). The NW axes are parallel to the [110] direction–perpendicular to the *c* axis. However, the SAED pattern of as-grown NWs exhibits multiple spots (inset of Figure 2c),

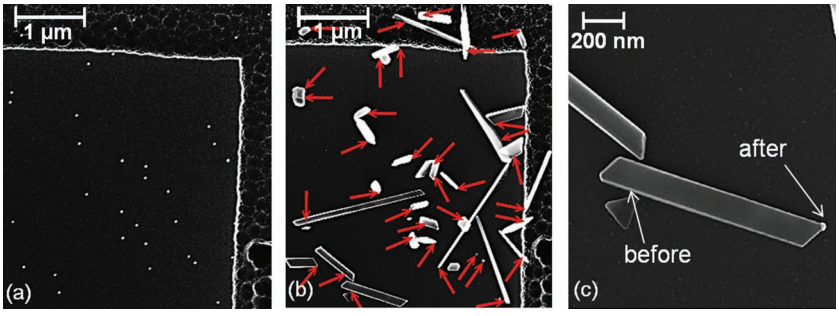

Figure 1. SEM images of: a) the distribution of gold nanoparticles (white spots) before deposition of bismuth telluride; b) the growth products after deposition of bismuth telluride for 5 min (the red arrows indicate the initial locations of the gold nanoparticles shown in (a)); and c) an enlarged part of the growth products shown at the bottom of (b).

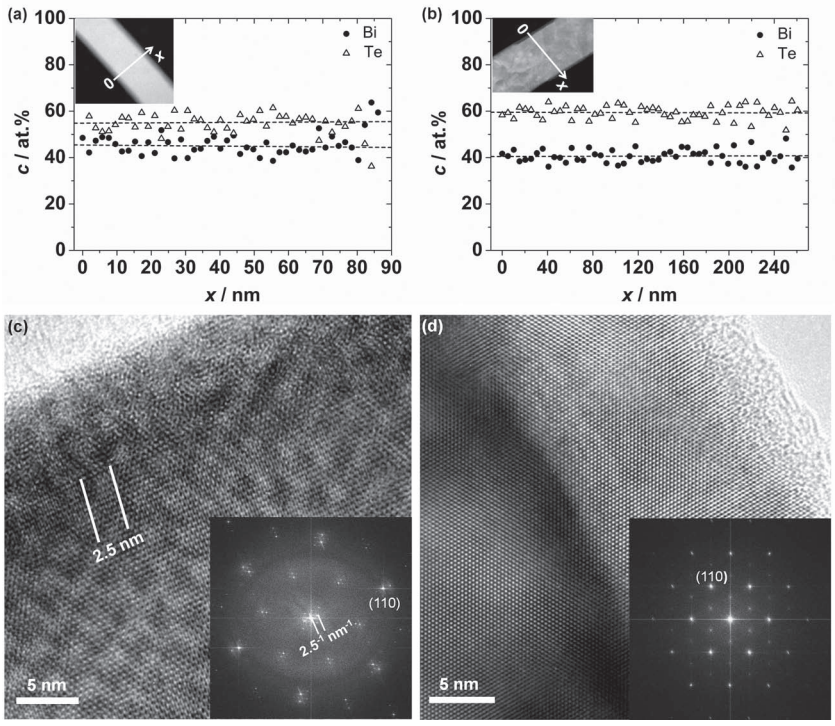

Figure 2. Representative compositional and structural results for as-grown nanowires (NWs) (a,c), and annealed NWs (b,d). The chemical compositions (a,b) were measured across the NW's cross-section, using EDX spectroscopy). The insets show high-angle annular dark-field scanning transmission electron microscopy (HAADF-STEM) images of the NWs indicating the EDX line-scans. The composition of as-grown NWs (a) clearly deviates from the Bi_2Te_3 phase, determined for annealed NWs (b). We observe Moiré patterns in the high-resolution transmission electron microscopy (HR-TEM) images of as-grown NWs (c), and multiple spots in the selected area electron diffraction (SAED) patterns (inset of (c)), which indicate a superlattice crystal structure. The HR-TEM images of the annealed NWs show a defect-free crystal structure (d), and the SAED patterns reveal single spots (inset of (d)), which indicates that the initial superlattice structure was removed during the annealing step.

which are particularly clear near the surfaces. This indicates a superlattice structure that could be related to the observed bismuth excess in that region. The superlattice structure leads to Moiré patterns in the corresponding HR-TEM images (Figure 2c). In contrast to the as-grown nanowires, the composition of annealed NWs appears uniform from the center of the NWs towards its sides with a ratio of Te to Bi atoms of 1.46 ± 0.13, which matches the stoichiometry of Bi_2Te_3 (Figure 2b). Moreover, no Moiré patterns are observed in the HR-TEM images (Figure 2d), and the SAED patterns of the annealed NWs reveal clear spots, even of higher order (inset of Figure 2d). This indicates that the initial superlattice structure was removed during the transformation to the Bi_2Te_3 phase.

The observed differences in crystal structure and chemical composition between as-grown and annealed NWs under Te atmosphere are mirrored in their thermoelectric properties. We determined the electrical conductivity σ and the Seebeck coefficient S for several individual as-grown and annealed NWs at room temperature. From both quantities the power factor, defined as $S^2\sigma$, can be determined. The cross-sectional areas of the NWs for calculating σ were determined using a scanning electron microscope in combination with scanning force microscopy. The Seebeck coefficients were measured relative to Pt, which has a negligible Seebeck coefficient.[37] The results are summarized in **Table 1**, along with

Table 1. Electrical conductivity σ, Seebeck coefficient S and power factor $S^2\sigma$ of individual as-grown and annealed bismuth telluride nanowires (NWs), measured at 300 K. The data of Zhou et al. and Mavrokefalos et al. were obtained for individual cylindrical, electrochemically grown NWs. The last two rows provide bulk values for comparison.

Composition	Cross-sectional area [nm^2]	σ [$\times 10^4\ \Omega^{-1}\ m^{-1}$]	S [$\times 10^{-6}$ V K^{-1}]	$S^2\sigma$ [$\times 10^{-4}$ W m^{-1} K^{-1}]	References
$Bi_{0.46\pm0.05}Te_{0.54\pm0.05}$	105 × 35	22.9 ± 1.8	−13.4 ± 1.6	0.4 ± 0.1	This work
(As-grown)	241 × 60	23.1 ± 1.3	−34.4 ± 1.4	2.7 ± 0.3	
	157 × 95	28.9 ± 1.8	−13.1 ± 1.1	0.5 ± 0.09	
	150 × 160	29.5 ± 2.1	−13.7 ± 1.03	0.6 ± 0.1	
$Bi_{0.41\pm0.03}Te_{0.59\pm0.03}$	108 × 47	2.10 ± 0.17	−89.1 ± 7.8	1.7 ± 0.3	This work
(Annealed)	120 × 48	1.68 ± 0.12	−128.7 ± 24.7	2.8 ± 1.1	
	389 × 48	2.08 ± 0.14	−140.8 ± 15.0	4.1 ± 0.9	
	96 × 60	2.05 ± 0.15	−156.9 ± 21.1	5.0 ± 1.4	
	π (64/2)^2	2.20 ± 0.69	−119.7 ± 6.4	3.2 ± 1.0	
	170 × 68	1.43 ± 0.08	−99.6 ± 5.2	1.4 ± 0.2	
$Bi_{0.54}Te_{0.46}$	π (81/2)^2	7	−9.4	0.06	Zhou et al.[10]
$Bi_{0.74}Te_{0.26}$	π (52/2)^2	21.5	−52	5.8	Mavrokefalos et al.[11]
Bi_2Te_3		6.9	−165.3	18.8	Bos et al.[9]
Bi_4Te_5	Bulk	52.4	−31.1	5.1	
Bi_6Te_7		26.8	−26.1	1.8	
Bi_8Te_9		26.2	−30.6	2.5	
BiTe		35.5	−28.9	3.0	
Bi_2Te_3	Nearly intrinsic bulk	1.4	–	–	Nolas et al.[1]

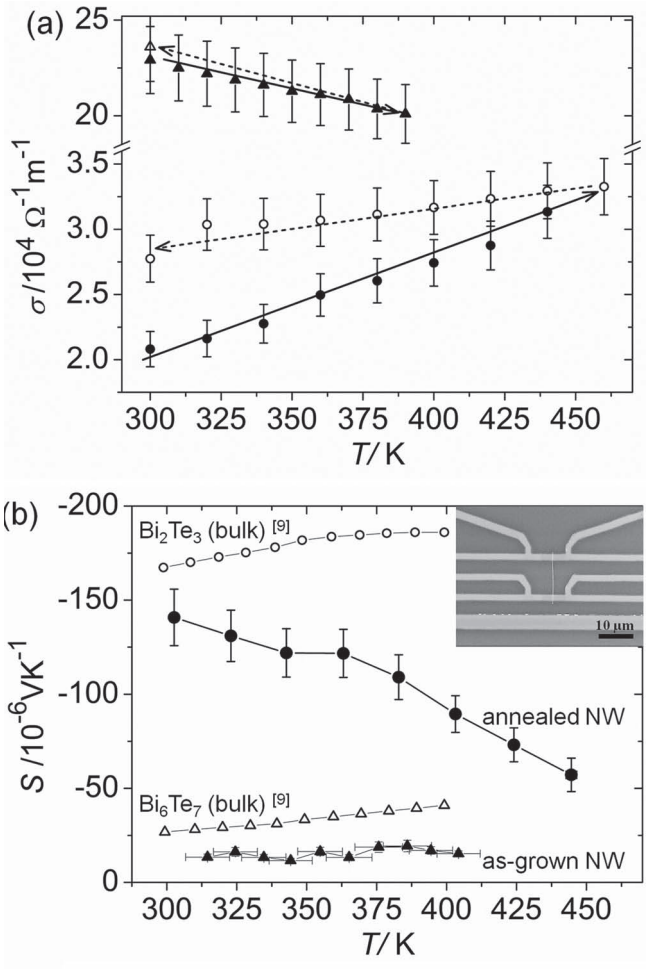

Figure 3. a) Temperature dependence of electrical conductivities, σ, of an as-grown NW (triangles) and an annealed NW (circles). The curves are irreversible during thermal cycling. The heating and cooling curves are indicated by the full and dashed arrows, respectively. The error bars are due to uncertainties in the determination of the sizes of the NWs. b) Temperature dependence of the Seebeck coefficients of an as-grown NW (filled triangles) and of an annealed NW (filled circles). The error bars are due to uncertainties in the determination of the temperature gradients. For the as-grown NW, due to the low *S*, a large temperature gradient was required, which increased the overall temperature of the NW, and led to large *x*-axis error bars. The inset shows a typical microdevice, including a heater-line and two four-point resistance thermometers, attached to a NW. For comparison, data from Bos et al., obtained for bulk Bi_2Te_3 (open circles) and for bulk Bi_6Te_7 (open triangles) are shown.[9]

literature values for electrochemically synthesized bismuth telluride NWs,[10,11] and bulk bismuth tellurides.[1,9,38] For the as-grown NWs we obtain mean values of $\sigma = (26.1 \pm 3.6) \times 10^4\ \Omega^{-1}\ m^{-1}$ and $S = (-18.6 \pm 1.5) \times 10^{-6}$ V K^{-1}, while for the annealed NWs σ is reduced and *S* is enhanced to mean values of $\sigma = (1.9 \pm 0.3) \times 10^4\ \Omega^{-1}\ m^{-1}$ and $S = (-122.5 \pm 25.3) \times 10^{-6}$ V K^{-1}, respectively. The observed changes of σ and *S* between the as-grown phase and the Bi_2Te_3 phase are comparable to those between bulk bismuth tellurides with Bi-contents above 40% and bulk Bi_2Te_3, although the bulk values of σ and *S* are larger (Table 1). However, the electrical conductivities measured on the annealed NWs are close to $\sigma = 1.4 \times 10^4\ \Omega^{-1}\ m^{-1}$, which has been obtained from the purest bulk Bi_2Te_3 specimens.[1,38] The enhanced values for σ and *S* reported for bulk specimens in work by Bos et al.[9] could be explained by the presence of antisite defects.[8]

The smallest geometric constriction of the investigated NWs (35 nm) lies well above 5 nm, below which quantum size effects may significantly enhance the power factor of Bi_2Te_3.[5] In the transition region between strong confinement and weak confinement (≈5 nm to ≈100 nm), calculations predict a decreasing power factor with decreasing diameter due to a decreasing number of nearly degenerate states.[39] Within the accuracy of our measurements, we observe no diameter or thickness dependency of the power factor. The temperature dependences of σ are depicted in **Figure 3**a, for representative NWs from each batch (as-grown and annealed). In non-stoichiometric Bi_2Te_3, the charge carrier density is dominated by antisite defects with donor and acceptor states close to the conduction and valence band edges, respectively.[8] The saturation range, in which all impurity states are activated, and in which intrinsic excitation of carriers is not yet significant, lies between about 100 K and about 300 K.[38,40] In this range, the electrical conductivity of bulk Bi_2Te_3 decreases with increasing temperature due to thermal scattering. With increasing defect density the saturation range is extended to higher temperatures. Likewise we observe monotonically decreasing electrical conductivities of as-grown NWs (Figure 3a). In contrast, the electrical conductivities of annealed NWs, when starting at room temperature, monotonically increase with temperature. This is consistent with the low electrical conductivity, and indicates small concentrations of antisite defects. However, as shown in Figure 3a, the electrical conductivity shows irreversible changes during thermal cycling: the cooling curve of the annealed NW shows still decreasing conductivities with decreasing temperatures, but the values lie above the previously recorded heating curve. A possible explanation could be diffusion into or from the contact leads at elevated temperatures, leading to extrinsic conduction, which superimposes the activation process of intrinsic conduction.

The respective temperature dependencies of the Seebeck coefficients are depicted in Figure 3b. The absolute Seebeck coefficient of as-grown NWs slightly increases, while the absolute Seebeck coefficient of annealed NWs monotonically decreases over the temperature range of the measurement due to an increasing bipolar contribution from both charge carrier types, thermally excited electrons and holes.

This work demonstrates the possibility of achieving nearly intrinsic single-crystalline Bi_2Te_3 NWs via VLS-growth and post-annealing in a Te atmosphere. The near intrinsic electrical conductivity makes the Bi_2Te_3 NWs promising candidates for investigating topological insulating effects. Regarding thermoelectricity, the Bi_2Te_3 NWs could be used as a well-defined starting system for enhancing the thermoelectric performance, for example, by nanoscale doping,[41] or by reduction of the cross-section area.[5]

Experimental Section

Substrate Preparation: Si substrates with native oxide layers were treated in a piranha solution (H_2SO_4:30% H_2O_2 = 3:1) at 90 °C for

15 min. Subsequently, the substrates were rinsed with isopropyl alcohol and deionized water, and dried using a nitrogen jet. The cleaned substrates were immersed in 0.1 wt% aqueous poly(L-lysine) solution (Ted Pella) for 60 s, and subsequently rinsed with deionized water. Finally the substrates were immersed in a solution containing gold nanoparticles (Ted Pella, diameter: 30nm) for 4 s. The negatively charged gold nanoparticles were spread evenly across the substrate surface due to attraction by the positive surface charges of the polymer film. The particle density was optimized to a value of about 0.5 μm^{-2}. After final rinsing with deionized water and drying with a nitrogen jet, the ready-prepared growth substrates were immediately mounted to the tube furnace for catalytic nanostructure growth.

Synthesis of Bi_2Te_3 Nanostructures: Bi_2Te_3 NWs were synthesized via physical vapor transport and gold-nanoparticle-assisted catalytic growth in a single heater zone tube furnace (MTI Inc. USA/OTF-1200X-25). The quartz tube of the furnace had a diameter of 25 mm and a length of 1 m. At the center of the tube furnace, 4 mg of Bi_2Te_3 powder was located for thermal evaporation. The growth substrate (Si with a native oxide layer, size: 30 mm x 10 mm x 530 µm, evenly covered with gold nanoparticles) was located at a distance of 20 cm to 23 cm from the center of the tube at the downstream zone of the furnace. Due to the inhomogeneous temperature profile across the tube furnace, the substrate temperature ranges from about 432 °C to about 355 °C. The charged furnace was evacuated to below 10 Torr and flushed several times with Ar gas to obtain an inert atmosphere. Then the Ar flow was adjusted to 30 sccm while the pressure was maintained at 10 Torr, and the base temperature was raised to 470 °C at a heating rate of 18 °C min^{-1}. After 1 h at 470 °C, the heating power was switched off. Under constant Ar flow and pressure, the furnace was returned to room temperature by natural cooling.

Annealing of the Growth Products: As-grown nanowires were annealed in Te atmosphere at 250 °C for 100 h. The annealing process was performed in a sealed evacuated quartz tube inside a tube furnace. More details about the annealing process can be found in work by Rostek et al.[32]

Structural and Compositional Characterization: The distribution of gold nanoparticles on the growth substrate, and the morphology of growth products were analyzed using a scanning electron microscope (Zeiss, Sigma Gemini). Additionally, the thicknesses of the NWs were determined by scanning force microscopy. Information about the chemical composition and the crystal structure, as well as a closer look at the morphology of NWs were obtained inside a transmission electron microscope (Titan 80-300). For quantifying the EDX spectra, we used the Bi-L (10.837 keV) and the Te-L (3.769 keV) X-ray peaks. We used the Cliff–Lorimer *k*-factors of 6.327 (Bi-L) and 3.311 (Te-L), which were calibrated by the manufacturer of the device.

Thermoelectric Measurements: Metal electrodes for current injection and voltage detection across our NWs were fabricated using a laser-lithography system (Heidelberg Instruments, µpg101) with a minimum line-width of 1 µm. In situ sputter-etching with Ar was used to remove any surface oxide on the NWs directly before sputter-deposition of Ti (4nm) and Pt (50 nm). This was followed by a lift-off process. In Figure S6a in the Supporting Information and in the inset of Figure 3b, a typical microdevice for measuring the electrical resistance and the Seebeck coefficient is depicted. The microdevice comprised two four-point resistance thermometers, which also served as voltage probes, and a heater line to generate a temperature gradient across the specimen of the order of 1 K. The microdevices were fabricated on Si substrates, insulated with 300 nm thermally grown SiO_2, as well as on glass substrates. Due to the smaller thermal conductivity of the latter, less heating power was required to reach the same temperature gradient, which was obtained using a Si/SiO_2 substrate. As shown in Figure S7 in the Supporting Information, the temperature at the thermometers (a), as well as the generated thermovoltage across the specimen (b), were proportional to the applied heating power. The determined electrical resistances included the contact resistances between metal electrode and NW. By comparison with four-probe measurements (Supporting Information, Figure S6b), we found that contact resistances were negligible (below 1% of the total resistances).

Supporting Information

Supporting Information is available from the Wiley Online Library or from the author.

Acknowledgements

B.H. and J.K. contributed equally to this work. This work was supported by the German science foundation (DFG) within the German priority program SPP 1386, "Nanostructured Thermoelectrics". We thank C. Schumacher, S. Bäßler, R. Meißner, and L. Akinsinde for technical support.

Received: June 18, 2012
Revised: September 6, 2012
Published online: November 2, 2012

[1] G. S. Nolas, J. Sharp, H. J. Goldsmid, in *Thermoelectrics* (Eds: A. Zunger, R. M. Osgood Jr., R. Hull, H. Sakaki), Springer-Verlag, Berlin Heidelberg, Germany **2001**, Ch. 5.
[2] H. Zhang, C.-X. Liu, X.-L. Qi, Z. Fang, S.-C. Zhang, *Nat. Phys.* **2009**, *5*, 438.
[3] Y. L. Chen, J. G. Analytis, J.-H. Chu, Z. K. Liu, S.-K. Mo, X. L. Qi, H. J. Zhang, D. H. Lu, X. Dai, Z. Fang, S. C. Zhang, I. R. Fisher, Z. Hussain, Z.-X. Shen, *Science* **2009**, *325*, 178.
[4] M. Z. Hasan, C. L. Kane, *Rev. Mod. Phys.* **2010**, *82*, 3045.
[5] L. D. Higgs, M. S. Dresselhaus, *Phys. Rev. B* **1993**, *47*, 16631.
[6] H. Peng, K. Lai, D. Kong, S. Meister, Y. Chen, X.-L. Qi, S.-C. Zhang, Z.-X. Shen, Y. Cui, *Nat. Mater.* **2009**, *9*, 225.
[7] D. M. Rowe, *CRC Handbook of Thermoelectrics*, CRC Press, Boca RatonFL, USA **1995**, Ch. 19.
[8] G. R. Miller, C.-Y. Li, *J. Phys. Chem. Solids* **1964**, *26*, 173.
[9] J. W. G. Bos, H. W. Zandbergen, M.-H. Lee, N. P. Ong, R. J. Cava, *Phys. Rev. B* **2007**, *75*, 195203.
[10] J. Zhou, C. Jin, J. H. Seol, X. Li, L. Shi, *Appl. Phys. Lett.* **2005**, *87*, 133109.
[11] A. Mavrokefalos, A. L. Moore, M. T. Pettes, L. Shi, W. Wang, X. Li, *J. Appl. Phys.* **2009**, *105*, 104318.
[12] S. A. Sapp, B. B. Lakshmi, Charles R. Martin, *Adv. Mater.* **1999**, *11*, 402.
[13] M. S. Sander, A. L. Prieto, R. Gronsky, T. Sands, A. M. Stacy, *Adv. Mater.* **2002**, *14*, 665.
[14] J. Lee, S. Farhangfar, J. Lee, L. Cagnon, R. Scholz, U. Gösele, K. Nielsch, *Nanotechnology* **2008**, *19*, 365701.
[15] R. Mannam, M. Agarwal, A. Roy, V. Singh, K. Varahramyan, D. Davis, *J. Electrochem. Soc.* **2009**, *156*, B871.
[16] O. Picht, S. Múller, I. Alber, M. Rauber, J. Lensch-Falk, D. L. Medlin, R. Neumann, M. E. Toimil-Molares, *J. Phys. Chem. C* **2012**, *116*, 5367.
[17] N. Peranio, E. Leister, W. Töllner, O. Eibl, K. Nielsch, *Adv. Funct. Mater.* **2012**, *22*, 151.
[18] C. Frantz, N. Stein, Y. Zhang, E. Bouzy, O. Picht, M. E. Toimil-Molares, C. Boulanger, *Electrochim. Acta* **2012**, *69*, 30.
[19] S. H. Kim, B. K. Park, *Mater. Lett.* **2010**, *64*, 938.
[20] A. Purkayastha, Q. Yan, M. S. Raghuveer, D. D. Gandhi, H. Li, Z. W. Liu, R. V. Ramanujan, T. Borca-Tasciuc, G. Ramanath, *Adv. Mater.* **2008**, *20*, 2679.
[21] R. J. Mehta, C. Karthik, W. Jiang, B. Singh, Y. Shi, R. W. Siegel, T. Borca-Tasciuc, G. Ramanath, *Nano Lett.* **2010**, *10*, 4417.
[22] J. Ham, W. Shim, D. H. Kim, S. Lee, J. Roh, S. W. Sohn, K. H Oh, P. W. Voorhees, and W. Lee, *Nano Lett.* **2009**, *9*, 2867.

[23] R. S. Wagner, W. C. Ellis, *Appl. Phys. Lett.* **1964**, *4*, 89.
[24] H. J. Fan, P. Werner, M. Zacharias, *Small* **2006**, *2*, 700.
[25] J. S. Lee, S. Brittman, D. Yu, H. Park, *J. Am. Chem. Soc.* **2008**, *130*, 6252.
[26] D. Kong, J. C. Randel, H. Peng, J. J. Cha, S. Meister, K. Lai, Y. Chen, Z.-X. Shen, H. C. Manoharan, Y. Cui, *Nano Lett.* **2010**, *10*, 329.
[27] R. B. Yang, J. Bachmann, E. Pippel, A. Berger, J. Woltersdorf, U. Gösele, K. Nielsch, *Adv. Mater.* **2009**, *21*, 1.
[28] G. Wang, S. K. Lok, G. K. L. Wong, I. K. Soua, *Appl. Phys. Lett.* **2009**, *95*, 263102.
[29] Q. Wei, Y. Su, C. J. Yang, Z. G. Liu, H. N. Xu, Y. D. Xia, J. Yin, *J. Mater. Sci.* **2011**, *46*, 2267.
[30] N. Han, S. I. Kim, J.-D. Yang, K. Lee, H. Sohn, H.-M- So, C. W. Ahn, K.-H-. Yoo, *Adv. Mat.* **2011**, *23*, 1871.
[31] J. Lee, A. Berger, L. Cagnon, U. Gösele, K. Nielsch, J. Lee, *Phys. Chem. Chem. Phys.* **2010**, *12*, 15247.
[32] R. Rostek, V. Sklyarenko, P. Woias, *J. Mater. Res.* **2011**, *26*, 1785.
[33] A. Prince, G. V. Raynor, D. S. Evans, *Phase Diagrams of Ternary Gold Alloy*, Institute of Metals, London **1990**, 172–178.
[34] S. Kodambaka, J. Tersoff, M. C. Reuter, F. M. Ross, *Science* **2007**, *316*, 729.
[35] D. Kong, W. Dang, J. J. Cha, H. Li, S. Meister, H. Peng, Z. Liu, Y. Cui, *Nano Lett.* **2010**, *10*, 2245.
[36] R. J. Mehta, Y. Zhang, C. Karthik, B. Singh, R. Siegel, T. Borca-Tasciuc, G. Ramanath, *Nat. Mater.* **2012**, *11*, 233.
[37] J. P. Moore, R. S. Graves, *J. Appl. Phys.* **1973**, *44*, 1174.
[38] H. J. Goldsmid, *Proc. Phys. Soc.* **1958**, *71*, 633.
[39] J. E. Cornett, O. Rabin, *Appl. Phys. Lett.* **2011**, *98*, 182104.
[40] J. P. Fleurial, L. Galliard, R. Triboulet, H. Scherrer, S. Scherrer, *J. Phys. Chem. Solids* **1988**, *49*, 1237.
[41] J. C. Ho, R. Yerushalmi, Z. A. Jacobson, Z. Fan, R. L. Alley, A. Javey, *Nat. Mater.* **2008**, *7*, 62.